

# Chapter 2

## Computational modelling of tissue ablation

### 2.1 Introduction and background

Lasers are used in wide variety of medical procedures not limited to: coagulating scalpels, port wine stain removal, tattoo removal, hair removal, and skin rejuvenation [16–20]. One class of laser used in these procedures are ablative lasers. Ablative lasers are usually high powered lasers targeted at a specific chromophore in the skin, to partially or fully remove layers of skin. These types of lasers are commonly used for aesthetic procedures such as: skin rejuvenation [20], and removal of various diseases such as Rhinophyma [21] or lesions/nodules [22]. They have also recently been investigated as a means of better drug delivery in the skin for [photo-dynamic therapy \(PDT\)](#) treatments [23].

One downside to using lasers to remove tissue, it that unlike a scalpel, where the surgeon has full control of the depth of the incision, ablative lasers are not as predictable. Lasers can also cause unwanted thermal damage to the surrounding areas, leading to unwanted effects.

Currently the only reliable method to measure the depth of the ablative holes, is via a biopsy, which is an invasive procedure. We propose to use [optical coherence tomography \(OCT\)](#) to measure the ablative crater non-invasively *in-vivo*. The [OCT](#) measurements are then backed up by a computational model. This computational model could then be used to predict the depth of the ablative crater when using a certain power for various different applications such as: laser assisted drug delivery, and various cosmetic applications.

This chapter examines using [MCRT](#) techniques coupled to a heat transfer simulation, in order to study the thermal damage to tissue due to fractional lasers. Fractionated ablative lasers are ablative lasers where the power is spread over several beams, such as to leave viable tissue around zones of damaged/necrotic tissue [24]. We present experimental work carried out by our collaborators at the University of Dundee and the photobiology department at Ninewells hospital, along side our computational model of tissue ablation.

### 2.2 Methods

In order to replicate the experimental work *in silico*, our numerical model has three main portions. The first is the [MCRT](#) that models light transport through tissue so that we can calculate the laser energy deposited as a function of time and space. The second, a [finite difference method](#)

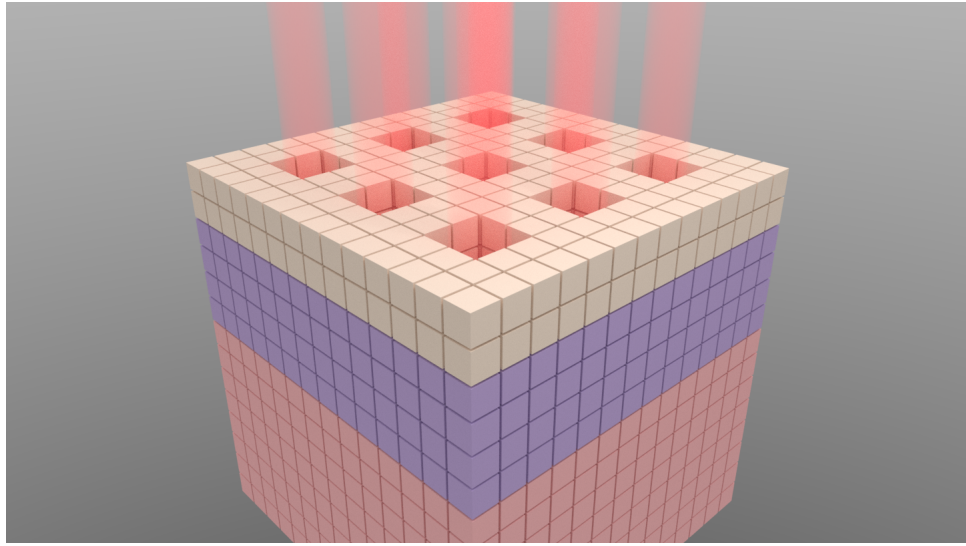


**Figure 2.1:** Example of a possible voxel model, with three different layers, various holes due to ablative pixel beam lasers. Each voxel represents a different optical/thermal property of the tissue medium.

(FDM) which is used to calculate the heat diffusion within the tissue due to the absorbed laser energy. Finally, a tissue damage model to track the damage to the tissue caused by the laser. All these individual portions are connected together to create our numerical model. Each portion of the numerical model is described below in more detail.

### 2.2.1 Monte Carlo radiation transport (MCRT)

MCRT is the ‘gold standard’ for simulating the transport of light through biological tissue [25]. This is due to its flexibility in modelling non standard geometries, and its ability to model various light sources and micro-physics, such as fluorescence. It uses interaction probabilities and random numbers in order to model the ‘random walk’ that photons undergo in a turbid medium. These ‘packets’ can undergo go scattering, absorption and various other physical process [26, 27]. MCRT has been used to model light-tissue interactions in many different medical and biophotonic applications [28–30]. MCRT is used here to calculate the energy deposited by the laser, which is then passed to the heat transport simulation.

The tissue medium for the MCRT and heat transport simulations is a 3D voxel model (Fig. 2.1). This allows the variation of optical and thermal properties from voxel to voxel, making it the ideal type of grid for modelling tissue ablation. We use  $80 \times 80 \times 80$  voxels \*still changing this\*, representing a tissue sample size of  $1.1 \times 1.1 \times 0.5$  cm. We assume the porcine skin is uniform, so that initially our voxel model is uniform, and the optical properties of porcine skin at the wavelength of interest is mainly that of water mixed with protein, see Fig. 2.10.

The original MCRT code was developed for astronomy applications [13, 31], and has since been adapted for medical applications [28, 32].

Figure 2.2. shows the overall algorithm for the simulation, including the MCRT portion. The MCRT portion of the algorithm begins with determining where the photon enters the medium. This is calculated by randomly selecting one of the pixel beams, from the  $9 \times 9$  array of pixel beams. Next the position on the surface of the medium is calculated. As the profile of the pixel

beams are unknown, they are assumed to be uniformly circular \*maybe change to gaussian??\*. Thus, the packets position is uniformly sampled on a circle the width of the pixel beam.

Once the packet enters the simulation, a propagation distance for the packets is calculated using Eq. (2.1). The packet then moves this distance before undergoing an interaction event. This can be either scattering or absorption, however in this simulation absorption dominates, and thus we assume no scattering takes place. This process is repeated until the photon has either been absorbed or exits the medium.

$$L = -\frac{\ln(\xi)}{\mu_a} \quad (2.1)$$

Where:

$\xi$  a random number ( $\tau = -\ln(\xi)$ ,  $\tau$  is the optical depth);

$\mu_a$  is the absorption coefficient;

$L$  is the physical distance.

Equation (2.1) is the equation for a uniform medium. As the medium we are simulating changes over time due to thermal damage this equation has to be adapted for a 3D Cartesian grid. Each voxel can have different optical properties, thus the photon packet is moved on a voxel by voxel basis. To start the movement process, a random number is generated, which is used to sample an optical depth the photon packet will travel. Next the photon enters the voxel and the maximum distance the photon can travel in the new voxel is calculated along the photons trajectory. If this optical distance is less than the optical depth sampled, then the photon enters the next voxel. If the distance is larger than the sampled optical distance then the photon has an interaction event in that voxel. The photon packet moves to the interaction event in the voxel and then undergoes scattering or absorption. The whole process is repeated until the photon ‘dies’ via absorption or leaving the medium. This in turn is again repeated for all the photons, until all the photons have been absorbed or have escaped the tissue medium. We use 1 million photons per MCRT simulation run.

To calculate the energy absorbed in the porcine tissue via the laser we use the path length counter method devised by Lucy [33]. Thus energy absorbed per voxel is calculated as:

$$E_i^{abs} = \frac{L}{N\Delta V_i} \sum \mu_a s \quad (2.2)$$

Where:

$L$  is luminosity [ $W$ ];

$N$  is the number of photons;

$\Delta V_i$  is the volume of the  $i^{th}$  voxel [ $m^{-3}$ ];

$\mu_{a,i}$  is the absorption coefficient of the  $i^{th}$  voxel [ $cm^{-1}$ ];

and  $s$  is the pathlength of a photon packet through the  $i^{th}$  voxel [ $cm$ ].

This grid of absorbed energy is then passed to the heat transport portion of the simulation, so that the heat diffusion can be calculated.

### 2.2.2 Heat transport

In order to model the transport of heat in porcine skin, we use the standard parabolic heat equation:

$$\rho c_p \frac{\partial T}{\partial t} = \nabla \cdot (\kappa \nabla T) + \dot{q} \quad (2.3)$$

Where:

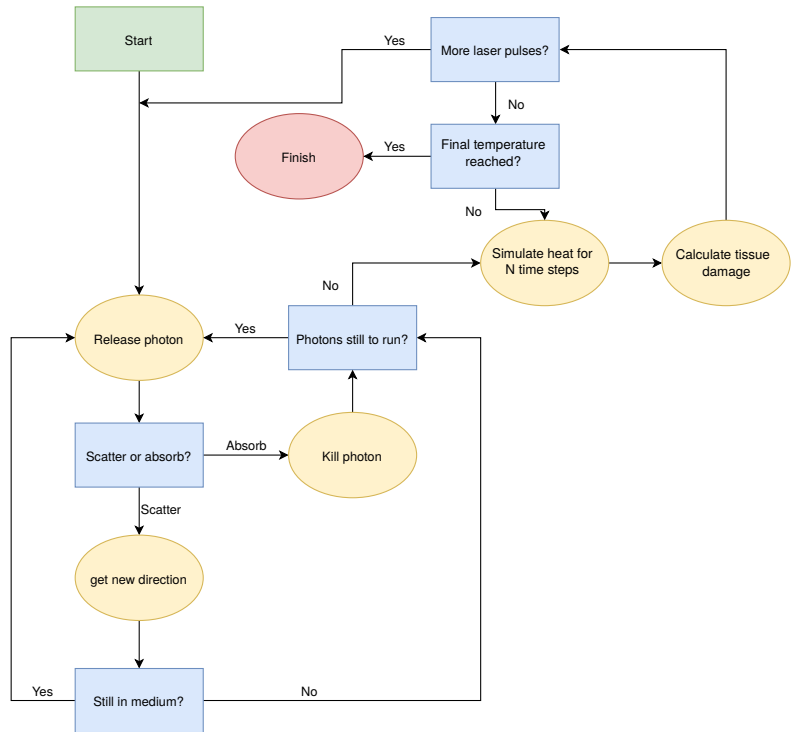


**Figure 2.2:** Flowchart of the tissue ablation algorithm.

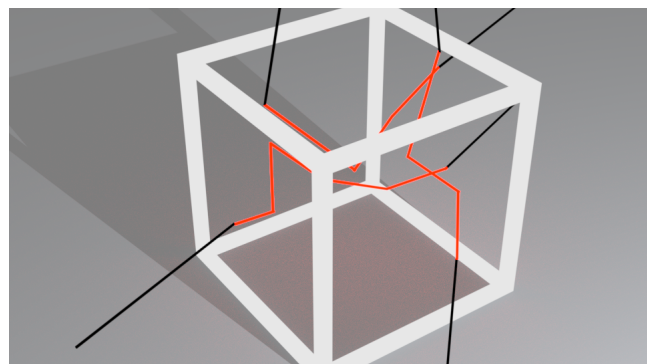


**Figure 2.3:** Red lines are photon paths within a voxel. Black lines photon paths outwith the voxel. Red photon paths are summed up in order to calculate the absorbed energy within each voxel.

$T(x, y, z, t)$  is the temperature as a function of time and space [K];  
 $\kappa$  is the thermal conductivity [ $W \cdot m^{-1} \cdot K^{-1}$ ];  
 $\rho$  is the density [ $Kg \cdot m^{-3}$ ];  
 $c_p$  the specific heat capacity [ $J \cdot K^{-1}$ ];  
 $\dot{q}(x, y, z, t)$  is the source/sink term as a function of time and space [ $W \cdot m^{-3}$ ].

As we are modelling a dynamic system, where the tissue's optical and thermal properties change as a function of space and time, we cannot make the assumption that  $\kappa$ ,  $\rho$ , and  $c_p$  are constant and thus we have to solve the non-linear heat equation (Eq. (2.4)).

$$\frac{\partial T}{\partial t} = \frac{1}{(\rho c_p)_\xi} (\nabla k_\xi T + k_\xi \nabla^2 T) + \dot{q} \quad \xi = (i, j, k) \quad (2.4)$$

The  $\dot{q}$  term is a heat source/sink term. The heat source in this simulation is due to the laser, and we assume the only loss of heat to the surrounding medium is via convection and conduction.

These boundary conditions must be considered. All faces of the cube, bar the laser facing face, are considered to be pinned at  $5^\circ C$ , as the porcine skin was kept cooled prior to experimental work and the simulation volume is smaller than the porcine tissue samples. The laser facing face has a simple convective BC:

$$\dot{q}_c = -hA(T - T_\infty) \quad (2.5)$$

Where:

$h$  is the heat transfer coefficient [ $W \cdot m^{-2} \cdot K$ ];  
 $A$  is the area of the grid element, that is radiating/convicting heat away [ $m^{-2}$ ];  
and  $T$ , and  $T_\infty$  are the temperature in a voxel and the surrounding medium temperature respectively [K].

As Eq. (2.4) is generally hard to solve in arbitrary geometries with complex boundary conditions we employ a numerical method to solve Eq. (2.4). The numerical method we employ is a **FDM**. The FDM is derived from the Taylor series approximation for derivatives. A function  $f(x)$  is discretised onto a grid with  $N$  nodes (see Fig. 2.4). Then at a node  $i$  we can use the Taylor series approximation in the forward (+ive  $x$  direction) and backward (-ive  $x$  direction) to give the derivatives in Eqs. (2.6a) and (2.6b). Where:  $i$  is the grid point at  $x_o$ ,  $i+1$  is the point at  $x_0 + \Delta x$ , and  $i-1$  is the grid point at  $x_0 - \Delta x$ . We can then combine these 'forward' and 'backward' derivatives to give a 'central' derivative Eq. (2.6c). We can also give expressions for the 2<sup>nd</sup> order derivatives for backward, forward and central (forward and backward 2<sup>nd</sup> order equations omitted for brevity) Eq. (2.6d).

$$\frac{df}{dx} = \frac{f_{i+1} - f_i}{\Delta x} \quad (forward) \quad (2.6a)$$

$$\frac{df}{dx} = \frac{f_i - f_{i-1}}{\Delta x} \quad (backward) \quad (2.6b)$$

$$\frac{df}{dx} = \frac{f_{i+1} - f_{i-1}}{2\Delta x} \quad (central) \quad (2.6c)$$

$$\frac{d^2f}{dx^2} = \frac{f_{i-1} - 2f_i + f_{i+1}}{\Delta x^2} \quad (central) \quad (2.6d)$$

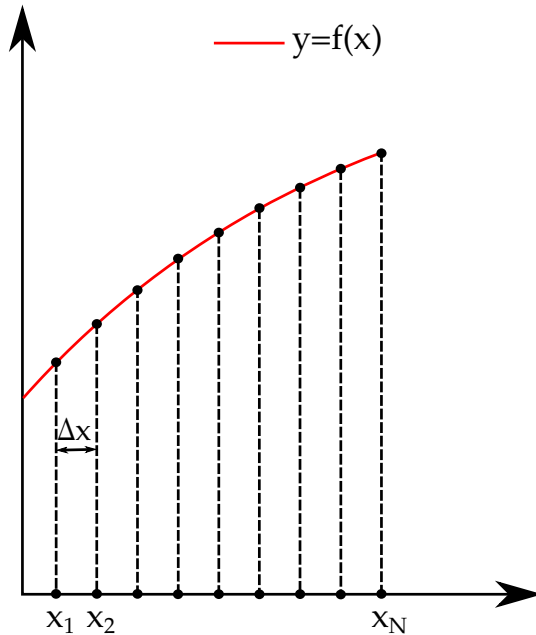


**Figure 2.4:** Discretisation of  $f(x)$ .

Thus the linear heat equation Eq. (2.3), in 1D, taking a  $1^{st}$  order forward time derivative, and a  $2^{nd}$  order central spatial derivative gives:

$$\frac{T_i^{n+1} - T_i^n}{\Delta t} = \alpha \frac{T_{i-1}^n - T_i^n + T_{i+1}^n}{\Delta x^2} + \frac{\dot{q}}{\rho c_p} \quad (2.7a)$$

$$T_i^{n+1} = \alpha \Delta t \frac{T_{i-1}^n - 2T_i^n + T_{i+1}^n}{\Delta x^2} + \frac{\dot{q}}{\rho c_p} \quad (2.7b)$$

Equation (2.7b) is called the ‘simple explicit form of finite-difference approximation’ [34]. Figure 2.5 shows the ‘stencil’ of this scheme, where there are three known points at time  $N$ , and just one unknown at time  $N+1$ . There are various other scheme that can be used to calculate

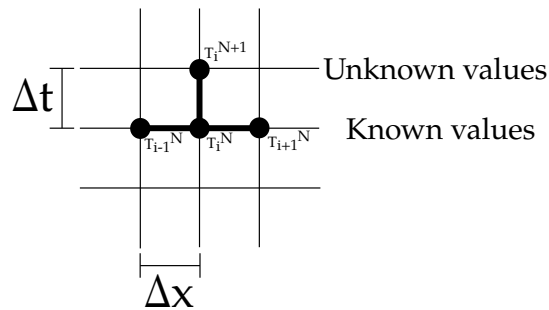


**Figure 2.5:** Finite difference method stencil for simple explicit scheme

the temperature at the next time step. However we use a simple explicit scheme here, due to its ease of implementation despite its stability being constrained in comparison to an implicit method. This method is also easily scaled up to 3D with little difficulty.

For the more complicated non-linear heat equation we have to account for the change of the medium between points in the space and time. The two easiest methods [34] of achieving this is: One, lag the value behind by one step, i.e  $c_p^{n+1} = c_p^n$ . Two, average  $\kappa$ ,  $\rho$ , and  $c_p$  using a half difference scheme:

$$\kappa^\pm = \frac{\kappa_i + \kappa_{i\pm 1}}{2} \quad (2.8)$$

$$\rho^\pm = \frac{\rho_i + \rho_{i\pm 1}}{2} \quad (2.9)$$

$$c_p^\pm = \frac{c_{p,i} + c_{p,i\pm 1}}{2} \quad (2.10)$$

Thus for the simple 1D case as in Eq. (2.7b), we average the thermal properties when computing the coefficients of the temperature nodes, and lag the thermal properties when adding the heat from the laser:

$$T^{N+1} = \Delta t (AT_{i-1}^N - 2BT_i^N + DT_{i+1}^N) + T_i^N + \frac{\dot{q}_L}{\rho c_p} \quad (2.11)$$

Where:

$$\begin{aligned} A &= \frac{\kappa^-}{\rho^- c_p^- 2\Delta x^2} \\ B &= \frac{\kappa^+}{\rho^+ c_p^+ 2\Delta x^2} \\ D &= \frac{(A + B)}{2} \end{aligned} \quad (2.12)$$

Equation (2.11) can be generalised to higher dimensions easily. The 3D case gives:

$$U_{xx} = (AT_{i-1,j,k}^N - 2BT_{i,j,k}^N + DT_{i+1,j,k}^N) \quad (2.13)$$

$$U_{yy} = (AT_{i,j-1,k}^N - 2BT_{i,j,k}^N + DT_{i,j+1,k}^N) \quad (2.14)$$

$$U_{zz} = (AT_{i,j,k-1}^N - 2BT_{i,j,k}^N + DT_{i,j,k+1}^N) \quad (2.15)$$

$$T_{i,j,k}^{N+1} = \Delta t (U_{xx} + U_{yy} + U_{zz}) + T_{i,j,k}^N + \frac{\Delta t}{\rho c_p} \dot{q}_L \quad (2.16)$$

Where:

$T_{i,j,k}^{N+1}$  is the new temperature at node  $i, j, k$  [ $K$ ];

$T_{i,j,k}^N$  is the temperature at node  $i, j, k$  at the current time step [ $K$ ];

$\alpha$  is the thermal diffusivity [ $m^2 \cdot s^{-1}$ ];

$\kappa$  is the thermal conductivity [ $W/m \cdot K$ ];

$\Delta x$  etc. is the size of the grid element in the  $p^{th}$  direction [ $m$ ];

and  $A, B, D$  are the coefficients in their respective dimension (Eq. (2.12)).

Incorporating B.Cs on the top air exposed face:

$$U_{zz} = \frac{\alpha}{\Delta z^2} \left( \frac{2\Delta z}{\kappa} (-h(T_{i,j,k}^N - T_\infty^N)) - 2T_{i,j,k}^N + 2T_{i,j,k+1}^N \right) \quad (2.17)$$

As the lasers \*maybe remove s?\* operate in a pulsed mode, we account for this in our simulation. We assume that the pulse shape is a top-hat pulse for simplicity. In the heat simulation we have an additional variable in the term  $\text{laserOn} \cdot \frac{\alpha\Delta t}{\kappa} q_L$  in Eq. (2.16). This additional variable,  $\text{laserOn}$ , is a boolean value, which is defined as:

$$\text{laserOn} = \begin{cases} 1, & \text{if time} \leq \text{pulse length} \\ 0, & \text{if time} > \text{pulse length.} \end{cases}$$

In the instance where there is more than one pulse, the laser is turned on and off based upon the pulse frequency.

As we are using a simple explicit FDM, the time step is constrained in order to make the solution stable. For a cubic 3D FDM without prescribed flux BCs, yields the constraint:  $\Delta t \leq \frac{\alpha\Delta x^2}{2\beta}$ . However as we have a flux prescribed boundary condition, the constraint on the time is more severe. Along with this time restraint, the pulse length of the laser also has to be considered. If the time step of the heat simulation is too large it will not account for the heat deposited by the laser. Thus, the timestep has to be an order of magnitude smaller than the shortest laser pulse.

As the timestep is small, and the grid resolution large, the resultant simulation is slow. Thus the code has been fully parallelised to improve performance. Both the MCRT and heat simulation are independently parallelised. As discussed in \*ref here\*, the MCRT simulation is fully parallelised, and the results are passed to the heat simulation.

Parallelisation of the heat simulation is more involved than the ‘embarrassingly parallel’ class of problems that MCRT belongs to. This is due to the heat simulation needing to know the temperature of adjacent nodes. Thus information will have to be passed from each individual core during computation, as opposed to doing the information passing at the end of the simulation à la MCRT parallelisation. The heat simulation is parallelised using a technique called ‘halo swapping’. This involves splitting up the computational domain (see Fig. 2.6), in this case the tissue medium, and doing the calculations on each domain on a separate core. The ‘halo swapping’ comes in when cores need to communicate with each other about updating their boundary temperature nodes (see Fig. 2.7).

On a workstation computer these simulations were carried out on (Intel Xeon E3-1245 v5, 8 core @ 3.5GHz) led to a speed up of ~6, over the serial simulation. Using Amdahl’s law [35], the serial portion of the simulation is ~ 5%, giving a theoretical speed up ~ 20 times the serial simulation.

After the heat transport has been completed, the grid of temperatures is passed to the tissue damage portion of the simulation.

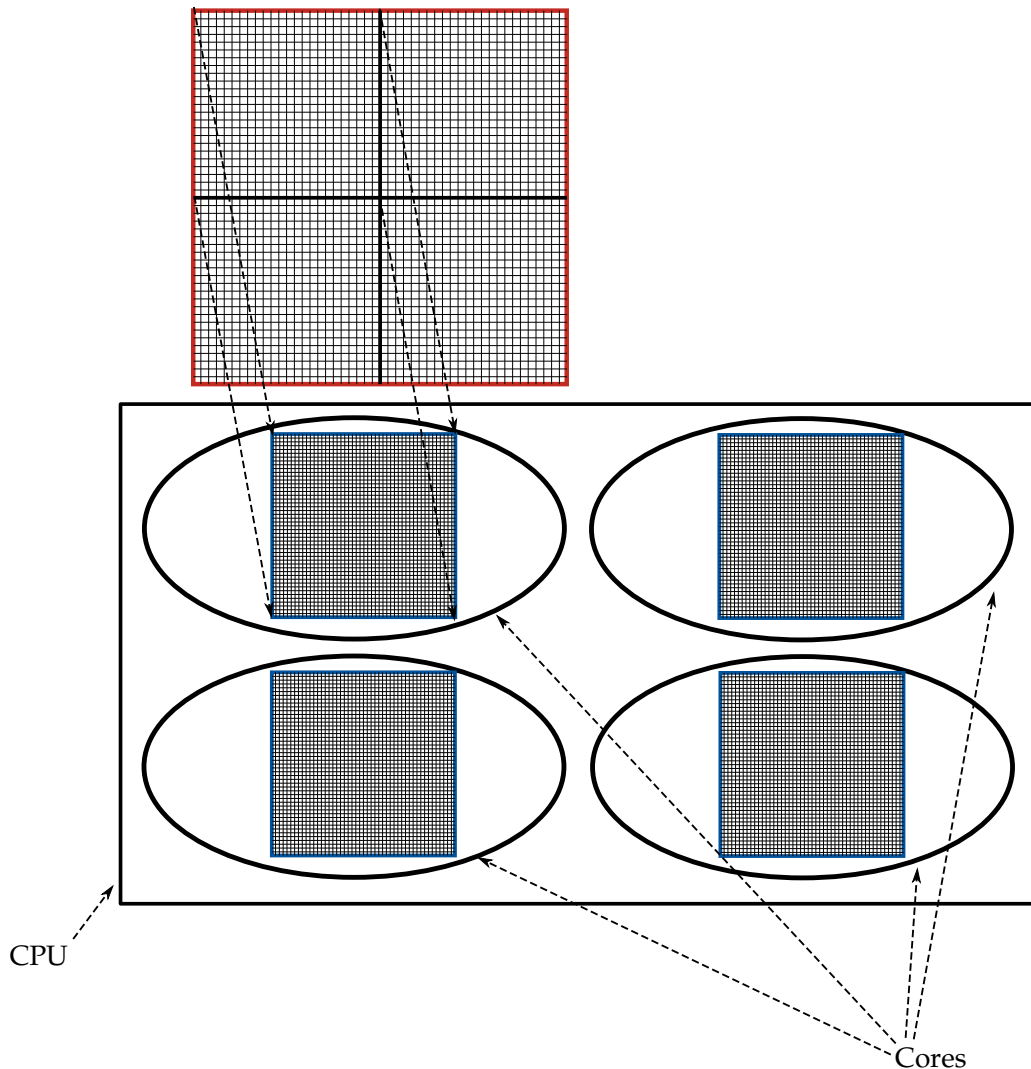


**Figure 2.6:** Computational domain decomposition. Total computational domain is evenly divided between cores in the CPU. This is done via layers of the domain in the  $z$  direction. Information is passed to/from cores via the ‘halo swap’ process (see Fig. 2.7).

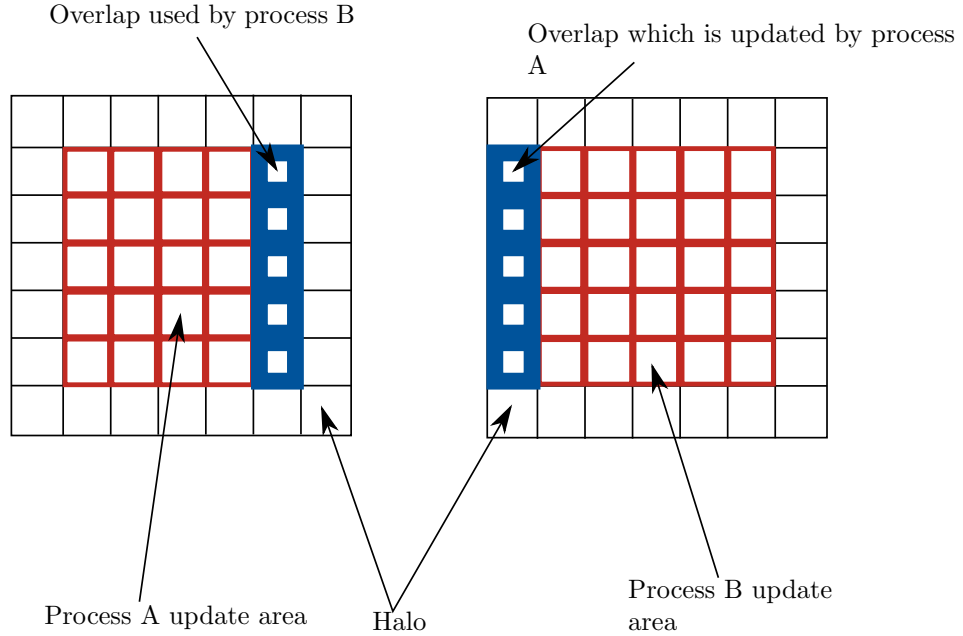


**Figure 2.7:** Halo swapping. Process A updates the area in red and blue on the left. It updates the blue area which is sent to process B as B's 'halo'. Process B cannot update its own halo, but rather updates the halo for process A.

## 2.2.3 Validation

### 2.2.3.1 Heat transport validation

In order to thoroughly validate the numerical method we employ to solve the heat equation, we compare the numerical method against an easily solvable case. We solve the heat equation on a cube, side L, in a surrounding medium of 0°C. The cube is initially at temperature 37°C and we calculate the temperature at time  $t=0.1s$ . Thus the boundary conditions are:

$$T(0, y, z, t) = T(x, 0, z, t) = T(x, y, 0, t) = 0^\circ\text{C} \quad (2.18)$$

$$T(L, y, z, t) = T(x, L, z, t) = T(x, y, L, t) = 0^\circ\text{C} \quad (2.19)$$

$$(2.20)$$

The thermal diffusivity ( $\alpha$ ), density ( $\rho$ ), and heat capacity ( $c_p$ ) are all set to 1. Assuming a separable solution in Cartesian coordinates for the heat equation yields:

$$\begin{aligned} T(x, y, z, t) = & (A_1 \cos(\alpha x) + A_1 \sin(\alpha x)) \cdot \\ & (B_1 \cos(\beta y) + B_1 \sin(\beta y)) \cdot \\ & (C_1 \cos(\gamma z) + C_1 \sin(\gamma z)) \cdot e^{-\alpha \mu^2 t} \end{aligned} \quad (2.21)$$

$$\mu^2 = \alpha^2 + \beta^2 + \gamma^2 \quad (2.22)$$

Applying the boundary conditions (Eqs. (2.18) and (2.19)) gives:

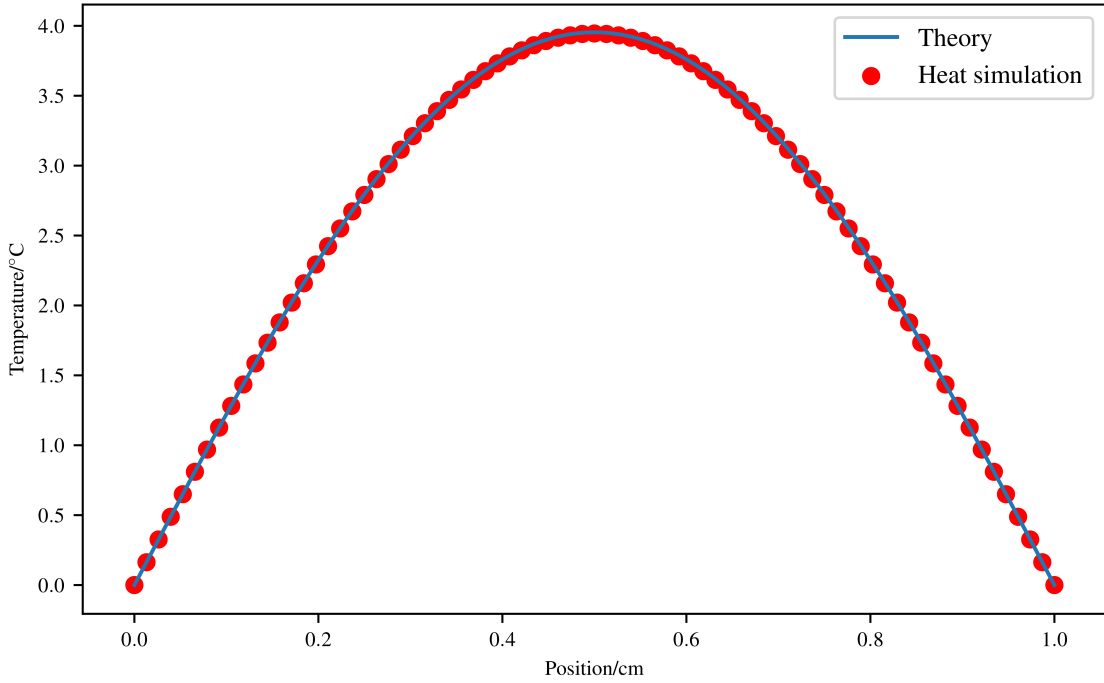


**Figure 2.8:** Comparison between analytical solution and numerical method.

$$A_1 = B_1 = C_1 = 0 \text{ and } \alpha = \frac{\pi n}{L}, \beta = \frac{\pi m}{L}, \gamma = \frac{\pi p}{L} \quad (2.23)$$

$$\therefore T_{nmp}(x, y, z, t) = A_{nmp} \sin\left(\frac{\pi n x}{L}\right) \cdot \sin\left(\frac{\pi m y}{L}\right) \cdot \sin\left(\frac{\pi p z}{L}\right) \quad (2.24)$$

This yields the following solution for the heat equation using the principle of superposition, and solving Eq. (2.25) with  $f(x, y, z)$  as the initial temperature profile of the cube:

$$A_{nmp} = \frac{8}{L^3} \int_0^L \int_0^L \int_0^L f(x, y, z) \cdot \sin\left(\frac{\pi n x}{L}\right) \cdot \sin\left(\frac{\pi m y}{L}\right) \cdot \sin\left(\frac{\pi p z}{L}\right) dx \cdot dy \cdot dz \quad (2.25)$$

$$T(x, y, z, t) = \sum_{n=1,3,\dots}^{\infty} \sum_{m=1,3,\dots}^{\infty} \sum_{p=1,3,\dots}^{\infty} \frac{2368}{\pi^3 nmp} \sin\left(\frac{\pi n x}{L}\right) \sin\left(\frac{\pi m y}{L}\right) \sin\left(\frac{\pi p z}{L}\right) e^{(-\lambda^2 t)} \quad (2.26)$$

Where:

$$\lambda^2 = \alpha \pi^2 \left( \frac{n^2}{L^2} + \frac{m^2}{L^2} + \frac{p^2}{L^2} \right);$$

$n, m, p$  are odd integers;

and  $L$  is the length of the cube.

At time,  $t = 0.1\text{s}$ , a slice through the middle of the cube,  $L = 1\text{ cm}$ , yields Fig. 2.8.

### 2.2.3.2 MCRT + heat transport validation

As a first test of our code, both **MCRT** and heat simulation, we compare to a simple analytical model of ablation. The simple model of ablation is as this: We define the ablation energy ( $E_a$ )

as the minimum energy required to raise the temperature of the medium to 100 °C, and then boil off the water in a volume  $dV$ , mass  $M$ . Thus in 1 dimension we have Eq. (2.27), where the symbols have their usual meanings. If the energy for ablation is delivered in a time  $dt$  by a laser of power density ( $W\text{cm}^{-2}$ ) this gives Eq. (2.28). Equation (2.28) can be rearranged in order to give an ablation front velocity, Eq. (2.29).

$$E_a = c_p \rho dx \Delta T + L_v \rho dx \quad (2.27)$$

$$P \cdot dt = \rho dx (c_p \Delta T + L_v) \quad (2.28)$$

$$u = \frac{P}{\rho(c_p \Delta T + L_v)} \quad (2.29)$$

Assuming the ablation front moves with constant velocity during the ablation, and using  $L_v = 2.53 \cdot 10^6 \text{ J} \cdot \text{Kg}^{-1}$ ,  $c_p = 4181 \text{ J} \cdot \text{Kg}^{-1} \cdot \text{K}^{-1}$  and the medium is a cube side 2 mm, with a starting temperature is 37 °C with a water content of 70% giving a density of 700  $\text{Kg} \cdot \text{m}^{-3}$ . For these parameter this gives an ablation velocity,  $u \simeq 0.77 \text{ cm} \cdot \text{s}^{-1}$ , and a time to ablate through 2 mm of  $t \simeq 0.26 \text{ s}$ . As the code developed in this chapter simulates the diffusion of heat in a medium due to an incident laser, the expected time to ablate through the same medium should be slightly less as heat diffuses away from the voxel while it is heated being heated. When the full heat + MCRT code is used to simulate this experiment, it gives a time,  $t \simeq 0.33 \text{ s}$ .

## 2.2.4 Tissue Damage

### 2.2.4.1 Introduction

The final portion of the simulation is the tissue damage model. To be able to model damage to the tissue we first need to be able to describe the tissue damage process due to heating from a laser.

When the laser is turned on, the temperature starts to rise within the tissue due to the absorption of photons by the tissue. The temperature rise causes damage to the tissue when above a threshold temperature,  $T_d$ , approximately 43°C [36]\*p539\*. From the temperature,  $T_d$ , we define four main areas of tissue damage:

$$T = \begin{cases} \text{coagulation,} & T_d \leq T \leq 100 \\ \text{water boils,} & T = 100 \\ \text{carbonisation,} & 100 \leq T \leq T_a \\ \text{ablation,} & T = T_a. \end{cases} \quad (2.30)$$

The area of tissue damage we term ‘coagulation’ is a multifaceted process. At 43°C - 50°C, bonds break within cell membranes, causing ruptures, and some cell death [36]. This process is usually termed *hyperthermia*. Around 50°C, enzyme activity decreases, cells become immobile, and various cell repair mechanisms are disabled, leading to more cell death. Temperatures of 60°C +, proteins become denatured. Thermal denaturation is a structural and functional change in a protein due to the heating it undergoes. This means they change from a highly organised structure with specific purposes, to disorganised structures with no function at all. A classic example of denaturation of proteins, is in cooking eggs. Denaturation occurs when the clear fluid egg white, rich in protein albumin, becomes a solid white [37].

The next stage in the tissue damage process is the vaporisation of water. As the temperature of the tissue starts to approach 100°C (at 1 atm), water starts to vaporise. If the vaporised water cannot escape the tissue it forms steam vacuoles, little pockets of steam. These vacuoles can

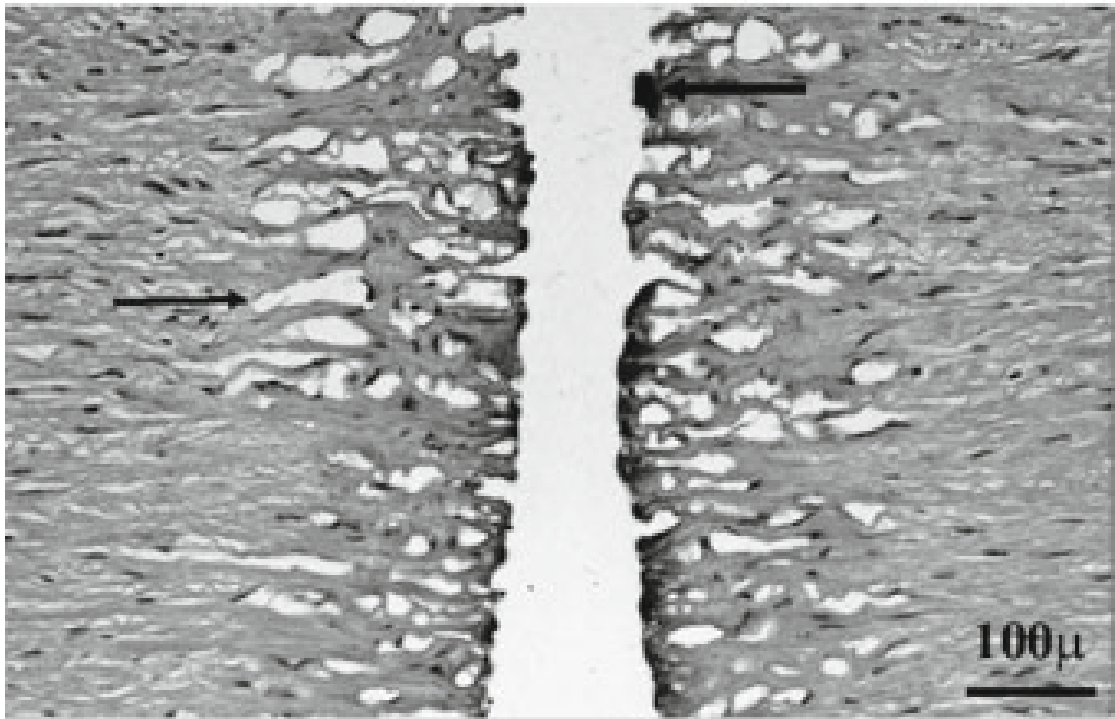


**Figure 2.9:** Tissue ablations, as viewed under a microscope. Steam vacuoles are clearly visible either side of the ablation area. Carbonisation is also evident at the edges of the ablation fronts. Adapted from [36].

easily been seen when viewing tissue samples after tissue has been treated with a high powered laser (see Fig. 2.9). In certain conditions these steam pockets can explode, with these ‘explosions’ being audible by the human ear [38].

The third stage of tissue damage is carbonisation or caramelisation of the tissue. This occurs when most of the water has boiled off, leaving the remaining tissue to heat up and reduce to its elemental carbon form. This carbonisation of tissue, when it occurs, is generally only a thin layer of 5-20  $\mu\text{m}$  [36].

The final stage of tissue damage is the removal of the remaining tissue, i.e tissue ablation. There is no agreement in the literature how tissue undergoes ablation with a number of methods proposed [39]. The tissue ablation process is not a simple process, with various unknowns which depend on everything from tissue composition to laser power and pulse length. The literature however, does suggest that it takes place when the tissue temperature is between 177 and 500°C [40, 41].

#### 2.2.4.2 Modelling coagulation damage

With the description of the various processes that tissue undergoes during ablation, we can now create a numerical model of these processes. First, in order to model the full extent of the damage done under 100°C, i.e in the coagulation regime, we use the Arrhenius damage model. The Arrhenius damage model was originally used as a kinetic model of reaction products in chemistry [42]. It has since been adapted by various authors for modelling tissue damage [43, 44]. These authors and various others, adapted this model by fitting Eq. (2.31) to experimental data for burn damage. The two parameters fitted in this way are the  $A$ , the frequency factor, and  $\Delta E$ ,

the activation energy.

$$\Omega(t) = \int_{t_i}^{t_f} A e^{-\frac{\Delta E}{RT}} d\tau \quad (2.31)$$

Where:

- $\Omega$  is the damage value;
- A is ‘frequency factor’ [ $s^{-1}$ ];
- $\Delta E$  is activation energy [ $J \cdot mol^{-1}$ ];
- R is the universal gas constant [ $J \cdot mol^{-1} \cdot K^{-1}$ ];
- T is the temperature [K];
- and  $t_i$  and  $t_f$  are the initial time and final time at  $t_{crit}$ .

It is reported that a value of  $\Omega$  of 0.53, 1.0, and  $10^4$  relate to first, second, and third degree burns respectively [45]. We use the Arrhenius damage model in order to better understand the amount of damage caused by the laser in the non-ablated areas of tissue. This can give us an insight into the various physical phenomena encountered in the OCT results.

#### 2.2.4.3 Modelling physical tissue damage

As tissue is generally mostly consists of water \*ref\* when the temperature of the tissue approaches 100°C (at 1 atm), water in the tissue begins to boil off. This acts as a large heat sink for the absorbed laser energy, slowing down the rate of ablation. The energy required to boil the water is  $Q_{vapor} = m_v \cdot L$ , where  $m_v$  is the mass of a voxel, and  $L$  is the latent heat of vaporisation. The energy to boil off the water is provided via the laser and heat diffusing into the voxel:

$$Q_{vapor} = \underbrace{laserOn \cdot \dot{q} \cdot \Delta t \cdot V_{i,j,k}}_{\text{laser heating}} + \underbrace{c \cdot M_{i,j,k} \cdot \Delta T}_{\text{heat diffusion}} \quad (2.32)$$

Where:

- $Q_{vapor}$  is the current energy in Joules that has been used to boil off the water in the voxel [J];
- $laserOn$  is a boolean variable that determine if the laser is on or off [-];
- $\dot{q}$  is the energy absorbed by the voxel due to the laser [ $W \cdot m^{-3}$ ];
- $\Delta t$  is the timestep [s];
- $V_{i,j,k}$  is the volume of the  $i^{th}$ ,  $j^{th}$ ,  $k^{th}$  voxel [ $m^3$ ];
- c is the heat capacity of the voxel [ $J \cdot K^{-1}$ ];
- $M_{i,j,k}$  is the mass of the  $i^{th}$ ,  $j^{th}$ ,  $k^{th}$  voxel [Kg];
- and  $\Delta T$  is the change in temperature the voxel would undergo, if the water was not boiling off.

As water boils off, the water content of each voxel changes. This affects the absorption coefficient, density, thermal conductivity, and heat capacity. Each of these vary linearly with water content per voxel [46];

$$W = W_{init} - \left( W_{init} \cdot \left( \frac{Q_{current}}{Q_{vaporisation}} \right) \right) \quad (2.33)$$

$$\rho = \frac{1000}{W + 0.649 \cdot P} \quad (2.34)$$

$$c_p = 4.2 \cdot 10^3 \cdot W + 1.09 \cdot 10^3 \cdot P \quad (2.35)$$

$$\kappa = \rho \cdot (6.28 \cdot 10^{-4} \cdot W + 1.17 \cdot 10^{-4} \cdot P) \quad (2.36)$$

$$\mu_a = W \cdot \mu_{water} + \mu_{protein} \quad (2.37)$$

$$(2.38)$$

Where:

$W$  is the water content (i.e  $W = 0.7$  equates to 70% water content);

$W_{init}$  is the initial water content;

$Q_{current}$  is the total energy absorbed by the  $i^{th}$  voxel since the temperature reached 100°C [J];

$P$  is the protein content (i.e  $P = 1.0 - W$ );

$\kappa$  is the Thermal conductivity [ $W \cdot m^{-1} \cdot K^{-1}$ ];

$c_p$  is the heat capacity [ $J \cdot Kg^{-1} \cdot K^{-1}$ ];

and  $\mu_a$  is the total absorption coefficient, and  $\mu_{water}$  and  $\mu_{protein}$  are the absorption coefficients of water and protein respectively.

We define the **ablation temperature ( $T_a$ )** as occurring between 177 and 500°C [40, 41]. At  $T_a$  the tissue is removed and the thermal, optical, and physical properties set to that of air.

The tissue structure is then fed back to the **MCRT** model and the whole process repeats until the predefined time limit is reached. This process is outlined in Fig. 2.2.

## 2.3 *In silico* results

### 2.3.1 Introduction

In order to match the experimental results, we must first create as accurate model of the experimental setup *in silico*. However due to computational constraints, such as memory and time available, we must make some approximations to the experimental setup. The porcine skin in reality was a large thin slice of the top most layers of the skin. However as the area of interest is where the ablation occurs, we model the porcine skin as a cuboid, dimensions: \*this will probably change\*  $1.1 \times 1.1 \times 0.5$  cm. The initial temperature of the porcine skin is assumed to be around 5°, as the tissue was kept on ice or was kept cooled. As mentioned in the previous sections, there are several unknowns in the model:  $T_a$ , water content, temperature of air after ablation, and the exact thermal and optical properties of the porcine tissue. Therefore we run several models so that the full parameter space of these unknowns can be explored. Results from these *in silico* experiments are presented in this section along with a comparison of the model to the experimental work carried out in collaboration with the University of Dundee and the photobiology department at Ninewells hospital.

#### 2.3.1.1 Optical & thermal properties

As mentioned, the thermal and optical properties of porcine tissue are not known exactly for a given tissue sample. This is due to no one tissue sample being exactly the same as another sample, due to various factors. As such the thermal and optical properties used in this section

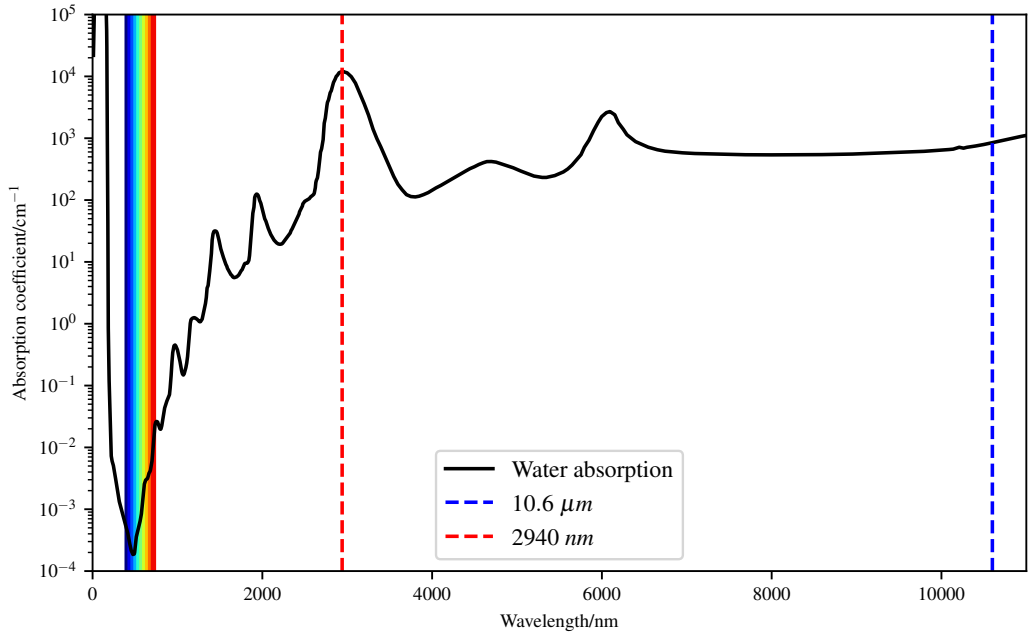


**Figure 2.10:** Water absorption coefficient for wavelengths 0-12000nm [47]. Data shows that water is highly absorbing in the infra-red portion of the spectrum.

	Thermal conductivity, $\kappa$	Density, $\rho$	Heat capacity, $c$
Tissue	$\rho \cdot (6.28 \cdot 10^{-4} \cdot W + 1.17 \cdot 10^{-4} \cdot P)$	$\frac{1000}{W+0.649 \cdot P}$	$4.2 \cdot 10^3 \cdot W + 1.09 \cdot 10^3 \cdot P$
Air	$a e^{-b(T-273.15)} + c$	$\frac{P_{atm}}{R_{spec} T}$	1006

**Table 2.1:** blah blah

are taken from various literature source and are modified over a range that is deemed acceptable according to various sources.

Both of the lasers used in the experimental work are infrared lasers, this means that the optical properties of the tissue are dominated by water absorption (see Fig. 2.10). The lasers used in the experiment are the Lynton lumina 576 Er:YAG, and the Pixel CO<sub>2</sub>. The Er:YAG laser has a wavelength 2940 nm which corresponds to an absorption coefficient of water:  $\sim 11200 \text{ cm}^{-1}$ . The CO<sub>2</sub> laser has a wavelength 10.6  $\mu\text{m}$  which corresponds to an absorption coefficient of  $\sim 850 \text{ cm}^{-1}$ . As the absorption coefficient is large, we assume that scattering is negligible at these wavelengths. Table 2.1 summarises the thermal properties for tissue and air used in the simulations.

Both lasers were used in ‘Pixel beam’ mode. This means that the laser beam is split into an array of smaller beams. The Er:YAG laser used a pattern of 5 x 5 lasers, with the corners missing, giving a total of 21 ‘Pixel beams’. The CO<sub>2</sub> laser used an array of 81 pixel beams with no missing ‘Pixels’. As the CO<sub>2</sub> laser was upgraded during the period in which the experimental data was taken, we present both sets of data, pre-upgrade and post-upgrade. The upgrade consisted of an update to the laser power, from 30 W to 70 W.

Both lasers operated in different modes; the Er:YAG delivered multiples pulses of either 350 mJ or 700 mJ, and the CO<sub>2</sub> delivered one single pulse of varying energy over the range

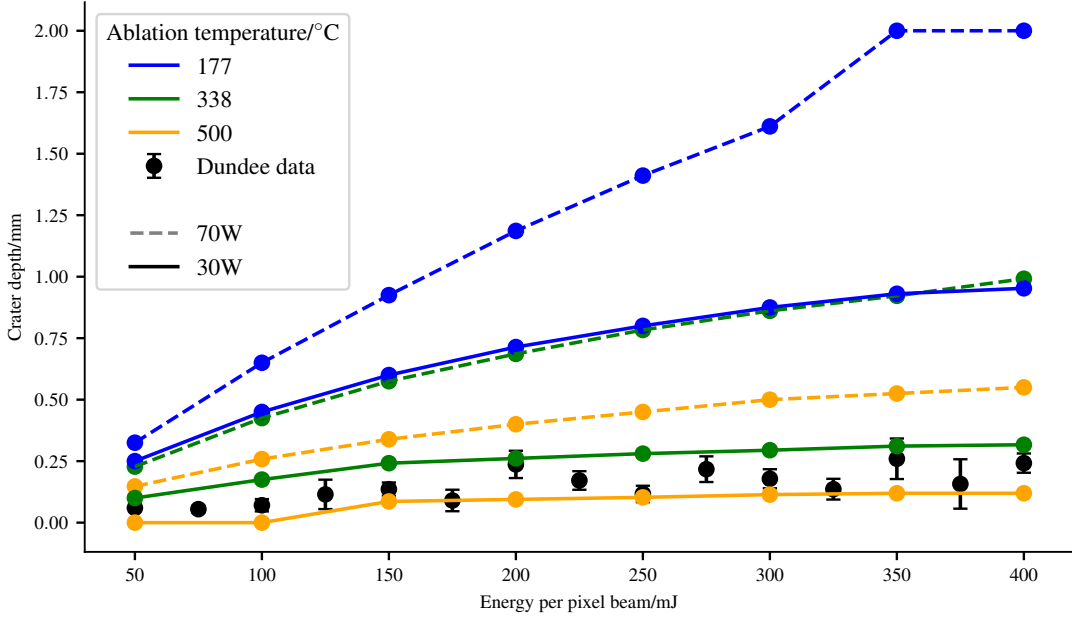


**Figure 2.11:** Simulations of 30 W and 70 W CO<sub>2</sub> ablative laser. Crater depths as a function of pixel beam energy for various  $T_a$ 's. \*placeholder until I get 70W dundee data. need to rerun the upper 177 points on larger z depth as it crashes currently\*

50 mJ to 400 mJ. The experiment consisted of ablating the porcine tissue, as a function of energy per ‘pixel’ beam. This was achieved by either stacking multiple pulses on top of each other for the Er:YAG laser over a range of 350 mJ to 3500 mJ. For the CO<sub>2</sub> the pulse length of each pulse was adjusted, so that the energy per pulse was varied over a range 50 mJ to 400 mJ. The energy range for the CO<sub>2</sub> laser was kept the same pre and post-upgrade.

### 2.3.1.2 Investigating ablation temperature, $T_a$

Various literature sources report the ablation temperature ranging from 177° to 500° [40, 41]. Thus, we run several models over this range in order to establish a ‘good’  $T_a$  to use for the rest of the simulations. Figure 2.11 shows how  $T_a$  affects the crater depth as a function of pixel beam energy for the CO<sub>2</sub> laser. Both the 70 W and 30 W simulations agree, that a ‘good’  $T_a$  is around  $T_a = 260^{\circ}\text{C}$ .

Increasing the ablation temperature, has the obvious affect of requiring more energy to be deposited by the laser before ablation takes place. As more energy is required to heat the porcine tissue upto the ablation temperature before it can be ablated.

### 2.3.1.3 Effect of thermal and optical properties on crater depth

As mentioned in the introduction to this section, the thermal and optical properties vary over a wide range in the literature. Thus there is no one ‘correct’ value we can choose for our simulations. In order to better understand how the thermal and optical properties affect the crater depth reached by the fractional laser, we vary the properties by 20%.

- 2.3.1.4** Investigating water content
- 2.3.1.5** Investigating temperature of air after ablation
- 2.3.1.6** Comparison to experimental work

## **2.4 Conclusion**

# Bibliography

- [1] Lee Badger. Lazzarini’s lucky approximation of  $\pi$ . *Mathematics Magazine*, 67(2):83–91, 1994.
- [2] Petr Beckmann. *A history of Pi*. St. Martin’s Griffin, 2015.
- [3] Georges-Louis Leclerc Buffon. *Histoire naturelle générale et particulière*, volume 18. de l’Imprimerie de F. Dufart, 1785.
- [4] Peter Jäckel. *Monte Carlo methods in finance*. J. Wiley, 2002.
- [5] David B Hertz. Risk analysis in capital investment. *Harvard Business Review*, 42(1):95–106, 1964.
- [6] Jasper Vivian Wall and Charles R Jenkins. *Practical statistics for astronomers*. Cambridge University Press, 2012.
- [7] James T. Kajiya. The rendering equation. *SIGGRAPH Comput. Graph.*, 20(4):143–150, August 1986.
- [8] Robert L. Cook, Thomas Porter, and Loren Carpenter. Distributed ray tracing. *SIGGRAPH Comput. Graph.*, 18(3):137–145, January 1984.
- [9] Nicholas Metropolis. The beginning of the Monte Carlo method. *Los Alamos Science*, 15:125–130, 1987.
- [10] Roger Eckhardt. Stan Ulam, John von Neumann, and the Monte Carlo method. *Los Alamos Science*, 15:131–136, 1987.
- [11] HL Anderson. Metropolis, Monte Carlo, and the MANIAC. *Los Alamos Science*, 14:96–108, 1986.
- [12] Stanislaw Ulam, RD Richtmyer, and J Von Neumann. Statistical methods in neutron diffusion. *LAMS-551, Los Alamos National Laboratory*, pages 1–22, 1947.
- [13] Kenneth Wood and RJ Reynolds. A model for the scattered light contribution and polarization of the diffuse  $h\alpha$  galactic background. *The Astrophysical Journal*, 525(2):799, 1999.
- [14] DWO Rogers, BA Faddegon, GX Ding, C-M Ma, J We, and TR Mackie. Beam: a monte carlo code to simulate radiotherapy treatment units. *Medical physics*, 22(5):503–524, 1995.
- [15] BC Wilson and G Adam. A monte carlo model for the absorption and flux distributions of light in tissue. *Medical Physics*, 10(6):824–830, 1983.

- [16] Saeid Amini-Nik, Darren Kraemer, Michael L Cowan, Keith Gunaratne, Puvindran Nadesan, Benjamin A Alman, and RJ Dwayne Miller. Ultrafast mid-ir laser scalpel: protein signals of the fundamental limits to minimally invasive surgery. *PLoS One*, 5(9):e13053, 2010.
- [17] Oon Tian Tan, Karen Sherwood, and Barbara A Gilchrest. Treatment of children with port-wine stains using the flashlamp-pulsed tunable dye laser. *New England journal of medicine*, 320(7):416–421, 1989.
- [18] Marina Kuperman-Beade, Vicki J Levine, and Robin Ashinoff. Laser removal of tattoos. *American journal of clinical dermatology*, 2(1):21–25, 2001.
- [19] Se Hwang Liew. Laser hair removal. *American journal of clinical dermatology*, 3(2):107–115, 2002.
- [20] Christina A Hardaway and E Victor Ross. Nonablative laser skin remodeling. *Dermatologic clinics*, 20(1):97–111, 2002.
- [21] Stanley M Shapshay, M Stuart Strong, Gaspar W Anastasi, and Charles W Vaughan. Removal of rhinophyma with the carbon dioxide laser: a preliminary report. *Archives of Otolaryngology*, 106(5):257–259, 1980.
- [22] Roberto Valcavi, Fabrizio Riganti, Angelo Bertani, Debora Formisano, and Claudio M Pacella. Percutaneous laser ablation of cold benign thyroid nodules: a 3-year follow-up study in 122 patients. *Thyroid*, 20(11):1253–1261, 2010.
- [23] Merete Hædersdal, Fernanda H Sakamoto, William A Farinelli, Apostolos G Doukas, Josh Tam, and R Rox Anderson. Fractional co<sub>2</sub> laser-assisted drug delivery. *Lasers in Surgery and Medicine: The Official Journal of the American Society for Laser Medicine and Surgery*, 42(2):113–122, 2010.
- [24] Dieter Manstein, G Scott Herron, R Kehl Sink, Heather Tanner, and R Rox Anderson. Fractional photothermolysis: a new concept for cutaneous remodeling using microscopic patterns of thermal injury. *Lasers in Surgery and Medicine: The Official Journal of the American Society for Laser Medicine and Surgery*, 34(5):426–438, 2004.
- [25] Rong Kong, Martin Ambrose, and Jerome Spanier. Efficient, automated monte carlo methods for radiation transport. *Journal of computational physics*, 227(22):9463–9476, 2008.
- [26] Gang Yao and Lihong V Wang. Monte carlo simulation of an optical coherence tomography signal in homogeneous turbid media. *Physics in Medicine & Biology*, 44(9):2307, 1999.
- [27] AJ Welch, Craig Gardner, Rebecca Richards-Kortum, Eric Chan, Glen Criswell, Josh Pfefer, and Steve Warren. Propagation of fluorescent light. *Lasers in Surgery and Medicine: The Official Journal of the American Society for Laser Medicine and Surgery*, 21(2):166–178, 1997.
- [28] Catherine Louise Campbell, Kenny Wood, RM Valentine, C Tom A Brown, and H Moseley. Monte carlo modelling of daylight activated photodynamic therapy. *Physics in Medicine & Biology*, 60(10):4059, 2015.
- [29] David A Boas, JP Culver, JJ Stott, and AK Dunn. Three dimensional monte carlo code for photon migration through complex heterogeneous media including the adult human head. *Optics express*, 10(3):159–170, 2002.

- [30] Sachin V Patwardhan, Atam P Dhawan, and Patricia A Relue. Monte carlo simulation of light-tissue interaction: three-dimensional simulation for trans-illumination-based imaging of skin lesions. *IEEE transactions on biomedical engineering*, 52(7):1227–1236, 2005.
- [31] Kenneth Wood, LM Haffner, RJ Reynolds, John S Mathis, and Greg Madsen. Estimating the porosity of the interstellar medium from three-dimensional photoionization modeling of h ii regions. *The Astrophysical Journal*, 633(1):295, 2005.
- [32] Isla Rose Mary Barnard, Patrick Tierney, Catherine Louise Campbell, Lewis McMillan, Harry Moseley, Ewan Eadie, Christian Tom Alcuin Brown, and Kenneth Wood. Quantifying direct dna damage in the basal layer of skin exposed to uv radiation from sunbeds. *Photochemistry and photobiology*.
- [33] LB Lucy. Computing radiative equilibria with monte carlo techniques. *Astronomy and Astrophysics*, 344:282–288, 1999.
- [34] Necati Ozisik. *Finite difference methods in heat transfer*. CRC press, 1994.
- [35] Gene M Amdahl. Validity of the single processor approach to achieving large scale computing capabilities. In *Proceedings of the April 18-20, 1967, spring joint computer conference*, pages 483–485. ACM, 1967.
- [36] Ashley J Welch, Martin JC Van Gemert, et al. *Optical-thermal response of laser-irradiated tissue*, volume 2. Springer, 2011.
- [37] Markolf H Niemz. *Laser-tissue interactions: fundamentals and applications*. Springer Science & Business Media, 2013.
- [38] Francesco Petrella, Sergio Cavaliere, and Lorenzo Spaggiari. Popcorn effect. *Journal of bronchology & interventional pulmonology*, 20(2):193–194, 2013.
- [39] Alfred Vogel and Vasan Venugopalan. Mechanisms of pulsed laser ablation of biological tissues. *Chemical reviews*, 103(2):577–644, 2003.
- [40] Miron Gerstmann, Y Linenberg, Abraham Katzir, and Solange Akselrod. Char formation in tissue irradiated with a co 2 laser: model and simulations. *Optical Engineering*, 33(7):2343–2352, 1994.
- [41] Alan L McKenzie. A three-zone model of soft-tissue damage by a co2 laser. *Physics in Medicine & Biology*, 31(9):967, 1986.
- [42] John A Pearce. Relationship between arrhenius models of thermal damage and the cem 43 thermal dose. In *Energy-based Treatment of Tissue and Assessment V*, volume 7181, page 718104. International Society for Optics and Photonics, 2009.
- [43] FC Jr Hendriques. Studies of thermal injury; the predictability and the significance of thermally induced rate processes leading to irreversible epidermal injury. *Arch. Pathol. (Chic)*, 43:489–502, 1947.
- [44] SC Jiang, N Ma, HJ Li, and XX Zhang. Effects of thermal properties and geometrical dimensions on skin burn injuries. *Burns*, 28(8):713–717, 2002.
- [45] KR Diller and LJ Hayes. A finite element model of burn injury in blood-perfused skin. *Journal of biomechanical engineering*, 105(3):300–307, 1983.

- [46] Bernard Choi and Ashley J Welch. Analysis of thermal relaxation during laser irradiation of tissue. *Lasers in Surgery and Medicine: The Official Journal of the American Society for Laser Medicine and Surgery*, 29(4):351–359, 2001.
- [47] David J Segelstein. *The complex refractive index of water*. PhD thesis, University of Missouri-Kansas City, 1981.